Chemical Science

ROYAL SOCIETY OF CHEMISTRY

EDGE ARTICLE

View Article Online
View Journal | View Issue

Cite this: *Chem. Sci.*, 2024, **15**, 1123

All publication charges for this article have been paid for by the Royal Society of Chemistry

Received 3rd October 2023
Accepted 24th November 2023

DOI: 10.1039/d3sc05220f

rsc.li/chemical-science

Mo-doping heterojunction: interfacial engineering in an efficient electrocatalyst for superior simulated seawater hydrogen evolution†

Zuo-Ming He,‡[ab] Chun-Xiao Zhang,‡[d] Si-Qi Guo,‡[e] Peng Xu,[a] Yuan Ji,[a] Si-Wei Luo,[a] Xiang Qi,[a] Yun-Dan Liu,*[a] Ning-Yan Cheng,*[e] Shi-Xue Dou,[f] Yun-Xiao Wang *[fg] and Bin-Wei Zhang *[bc]

Exploring economical, efficient, and stable electrocatalysts for the seawater hydrogen evolution reaction (HER) is highly desirable but is challenging. In this study, a Mo cation doped $Ni_{0.85}Se/MoSe_2$ heterostructural electrocatalyst, Mo_x-$Ni_{0.85}Se/MoSe_2$, was successfully prepared by simultaneously doping Mo cations into the $Ni_{0.85}Se$ lattice (Mo_x-$Ni_{0.85}Se$) and growing atomic $MoSe_2$ nanosheets epitaxially at the edge of the Mo_x-$Ni_{0.85}Se$. Such an Mo_x-$Ni_{0.85}Se/MoSe_2$ catalyst requires only 110 mV to drive current densities of 10 mA cm^{-2} in alkaline simulated seawater, and shows almost no obvious degradation after 80 h at 20 mA cm^{-2}. The experimental results, combined with the density functional theory calculations, reveal that the Mo_x-$Ni_{0.85}Se/MoSe_2$ heterostructure will generate an interfacial electric field to facilitate the electron transfer, thus reducing the water dissociation barrier. Significantly, the heteroatomic Mo-doping in the $Ni_{0.85}Se$ can regulate the local electronic configuration of the Mo_x-$Ni_{0.85}Se/MoSe_2$ heterostructure catalyst by altering the coordination environment and orbital hybridization, thereby weakening the bonding interaction between the Cl and Se/Mo. This synergistic effect for the Mo_x-$Ni_{0.85}Se/MoSe_2$ heterostructure will simultaneously enhance the catalytic activity and durability, without poisoning or corrosion of the chloride ions.

Introduction

Hydrogen fuel is considered as an ideal alternative to traditional fossil resources due to its superior energy density of 142 kJ g^{-1} and its environmentally friendly nature.[1–3] Water splitting is an economical strategy to generate hydrogen. However, current mature water electrolysis technology typically relies on high-purity water.[4,5] If this water electrolysis were to be commercialized, it would place a significant strain on freshwater resources.[6] Seawater, which accounts for approximately 96.5% of the Earth's water,[7] shows promise as a natural electrolyte. Nevertheless, direct seawater electrolysis is still in its early stages and faces significant challenges, including the poisoning effect of non-innocent ions such as chlorine anions, and the low kinetics of the hydrogen evolution reaction (HER).[8–10] Furthermore, these will occur in the chlorine evolution reaction (CER) in an acid environment, and they compete with the oxygen evolution reaction (OER).[11] It is widely accepted that in alkaline conditions, the CER can be efficiently blocked, and the OER usually exhibits a reasonable performance.[12,13] Moreover, the possibility of seawater splitting in alkaline conditions has been widely demonstrated in recent years.[13–15] Platinum (Pt)-based materials are regarded as the state-of-art HER catalysts,[16,17] however, the scarcity and expensiveness of Pt limit its wide application.[18–20] In addition, the presence of chlorine anions in seawater will also poison Pt-based catalysts, which decreases the electrochemical performance for seawater splitting.[21] Therefore, it is crucial to explore earth-abundant, efficient, and non-poisonous electrocatalysts for HERs in seawater.

A great deal of effort has been made in developing efficient non-precious HER electrocatalysts over the past several

[a]*Hunan Key Laboratory of Micro-Nano Energy Materials and Devices, Xiangtan University, Xiangtan 411105, PR China. E-mail: liuyd@xtu.edu.cn*

[b]*School of Chemistry and Chemical Engineering, Chongqing University, Chongqing 400044, PR China. E-mail: binwei@cqu.edu.cn*

[c]*Center of Advanced Electrochemical Energy, Institute of Advanced Interdisciplinary Studies, Chongqing 400044, PR China*

[d]*School of Physics and Optoelectronic Engineering, Shandong University of Technology, Zibo 255000, PR China*

[e]*Information Materials and Intelligent Sensing Laboratory of Anhui Province, Key Laboratory of Structure and Functional Regulation of Hybrid Materials of Ministry of Education, Institutes of Physical Science and Information Technology, Anhui University, Hefei 230601, PR China. E-mail: ningyancheng@ahu.edu.cn*

[f]*Institute of Energy Materials Science (IEMS), University of Shanghai For Science and Technology, Shanghai, 200093, China*

[g]*Institute for Superconducting and Electronic Materials, Australian Institute of Innovative Materials, University of Wollongong, North Wollongong, New South Wales 2500, Australia. E-mail: yunxiao@uow.edu.cn*

† Electronic supplementary information (ESI) available. See DOI: https://doi.org/10.1039/d3sc05220f

‡ These authors contributed equally: Z. M. He, C. X. Zhang, S. Q. Guo.

decades.[22–24] Among these candidates, transition-metal chalcogenide heterostructural electrocatalysts have attracted significant attention due to their lower cost and outstanding electrochemical properties.[25–27] For example, Ni-based heterogeneous catalysts have attracted much attention as they have strong interfacial effects and unique electronic structures.[28] Although significant research has been made to improve the activity of HER, Ni-based selenides still suffer from the poisoning of the chlorine ions and poor stability.[29] However, the use of $MoSe_2$ as a HER catalyst has been extensively investigated because of its low Gibbs' free energy for hydrogen adsorption on the Mo-edge of $MoSe_2$.[30,31] Thus, rational integration of $NiSe_x$ and $MoSe_2$ to construct a heterostructure can optimize the electrocatalytic activity for HER.[32] However, to the best of our knowledge, so far, the corresponding work on the $NiSe_x/MoSe_2$ heterostructures as HER electrocatalysts in the seawater environment has seldom been studied in detail.

In this work, novel Mo_x-$Ni_{0.85}Se/MoSe_2$ heterostructures were successfully achieved using the edge epitaxy of atomic $MoSe_2$ nanosheets on Mo-doped $Ni_{0.85}Se$ using a one-pot selenization process of the precursor $NiMoO_4$ nanosheets. Such Mo_x-$Ni_{0.85}Se/MoSe_2$ heterostructures exhibited efficient electrocatalytic behavior in alkaline simulated seawater, with a low overpotential of 110 mV at 10 mA cm^{-2}. Significantly, the Mo_x-$Ni_{0.85}Se/MoSe_2$ catalyst could be effective against the poisoning and corrosion of chloride ions, and displayed an impressive electrochemical stability over 80 h in alkaline simulated seawater. A deep insight into the outstanding electrochemical performance mechanism was obtained that showed that the built-in interfacial electric field of the Mo_x-$Ni_{0.85}Se/MoSe_2$ heterostructure would improve the charge transfer, and that the Mo cation could modify the local electronic environment of $Ni_{0.85}Se$ *via* the formation of sp^3d^2 hybridization in the Ni–Se octahedral geometry, and sp^3d hybridization in the Mo–Se square pyramidal geometry, thus weakening the bonding interaction between the Cl–Se and Cl–Mo.

Results and discussion

Synthesis and characterization of Mo_x-$Ni_{0.85}Se/MoSe_2$

The Mo_x-$Ni_{0.85}Se/MoSe_2$ heterostructures anchored on carbon cloth (CC) were prepared by hydrothermal selenization of $NiMoO_4$ with adding Ni sources, a reducing agent ($NaBH_4$), and additional Mo sources, as shown in Fig. 1a. Scanning electron microscopy (SEM) images (Fig. S1, ESI†) and X-ray diffraction spectra (XRD, Fig. S2, ESI†) of $NiMoO_4$ nanosheets indicated that they were vertically supported on a carbon fiber with a highly open structure made up of interwoven nanosheets. To optimize the morphology and performance, a series of different amounts of additional Mo sources were employed during the hydrothermal selenization process (Fig. S3, ESI†). It was clearly seen that when the weight of $Na_2MoO_4 \cdot 2H_2O$ was below 60 mg, the obtained samples could maintain the nanosheet structure. When the additional weight of $Na_2MoO_4 \cdot 2H_2O$ was 60 mg, the obtained sample (named as Mo_x-$Ni_{0.85}Se/MoSe_2$) shows a thin nanosheet structure (Fig. 1b, S3e and f, ESI†). When adding excess Mo sources, a large number of nanoparticles accumulated. Their HER performance was studied and the results are shown in Fig. S4 (ESI),† and the Mo_x-$Ni_{0.85}Se/MoSe_2$ showed the best HER performance among these samples.

High-angle annular dark-field scanning transmission electron microscopy (HAADF-STEM) images of Mo_x-$Ni_{0.85}Se/MoSe_2$ (Fig. 1c) showed the epitaxially grown heterostructure of $Ni_{0.85}Se/MoSe_2$, *i.e.*, the epitaxially growing atomic $MoSe_2$ nanosheets at the edge of the $Ni_{0.85}Se$ nanoparticles. It was clearly seen that the epitaxial growth of a few atomic layers of $MoSe_2$ corresponded with elemental mapping results (Fig. 1d). The high-resolution STEM (HR-STEM) image clearly showed the lattice fringes of the inter-nanoparticle with a spacing of 0.20 and 0.18 nm, which corresponded to the (102) and (110) crystal planes of the $Ni_{0.85}Se$, respectively. This result also demonstrated the heterostructure of the $Ni_{0.85}Se/MoSe_2$. Additionally, the HAADF-STEM image of Mo_x-$Ni_{0.85}Se/MoSe_2$ in Fig. 1e also shows bright dots in the $Ni_{0.85}Se$ nanoparticles. As the atomic number of Mo was the highest among these three elements, the bright dots could be attributed to Mo. Thus, it was concluded that the $Ni_{0.85}Se$ nanoparticles had been doped by the Mo cations. The model of the Mo cation doping Mo_x-$Ni_{0.85}Se$ was also identified by simulating its atomic resolution HR-STEM image using QSTEM software (Fig. 1e–g and S5, ESI†).[33] The Mo cation doping is circled in yellow in Fig. 1e–g. These results also demonstrate the Mo cation doping of the Mo_x-$Ni_{0.85}Se$ structure. We also prepared pure $NiSe_2$ and $MoSe_2$ as comparison and the results are shown in Fig. S6 and S7 (ESI).† Then, the XRD of these samples were employed to investigate their crystal structure and phase composition. As shown in Fig. S8 (ESI),† the two distinct peaks at about 26° and 43° were assigned to the carbon cloth. It was also noted that the $MoSe_2$ exhibited an amorphous structure, which also suggested its atomic layer structure. The peaks of $NiSe_2$ were in agreement with the standard card of $NiSe_2$ (PDF#65-1843). The Mo_x-$Ni_{0.85}Se/MoSe_2$ also presented the typical $Ni_{0.85}Se$ (PDF#18-0888), but the peak of (101) at 33.5° was positive shifted, indicating the successful Mo cation doping in the lattice of $Ni_{0.85}Se$. To characterize the composition in the heterojunction, the Raman spectra were utilized and are shown in Fig. S9 (ESI).† The peak (A_g) at 237 cm^{-1} was attributed to the Se–Se stretching mode of $NiSe_2$.[34] The Mo_x-$Ni_{0.85}Se/MoSe_2$ presented three peaks of 139, 235, and 284 cm^{-1}, which were attributed to the phonon mode of $MoSe_2$.[35] In addition, there was also a faint peak at ~510 cm^{-1}, which was attributed to the unique stretch mode of the Ni–Se of $Ni_{0.85}Se$ with a hexagonal structure.[34]

Synchrotron X-ray absorption spectroscopy (XAS) (Fig. 2a–h) was performed to further investigate the charge states and the local structure of Mo_x-$Ni_{0.85}Se/MoSe_2$. Fig. 2a shows the Ni K-edge X-ray absorption near edge structure (XANES) spectra for Mo_x-$Ni_{0.85}Se/MoSe_2$, $NiSe_2$, and Ni foil. It can be clearly seen that the white-line intensity of Mo_x-$Ni_{0.85}Se/MoSe_2$ was much lower than that of $NiSe_2$, suggesting that its chemical state was lower than that of $NiSe_2$. In addition, the Mo_x-$Ni_{0.85}Se/MoSe_2$ also shifted to a higher energy than the Ni foil, revealing that it had a higher chemical valence than Ni^0. These results demonstrated that the Ni chemical state of Mo_x-$Ni_{0.85}Se/MoSe_2$ was between 0 and +2. Fourier transform extended X-ray absorption

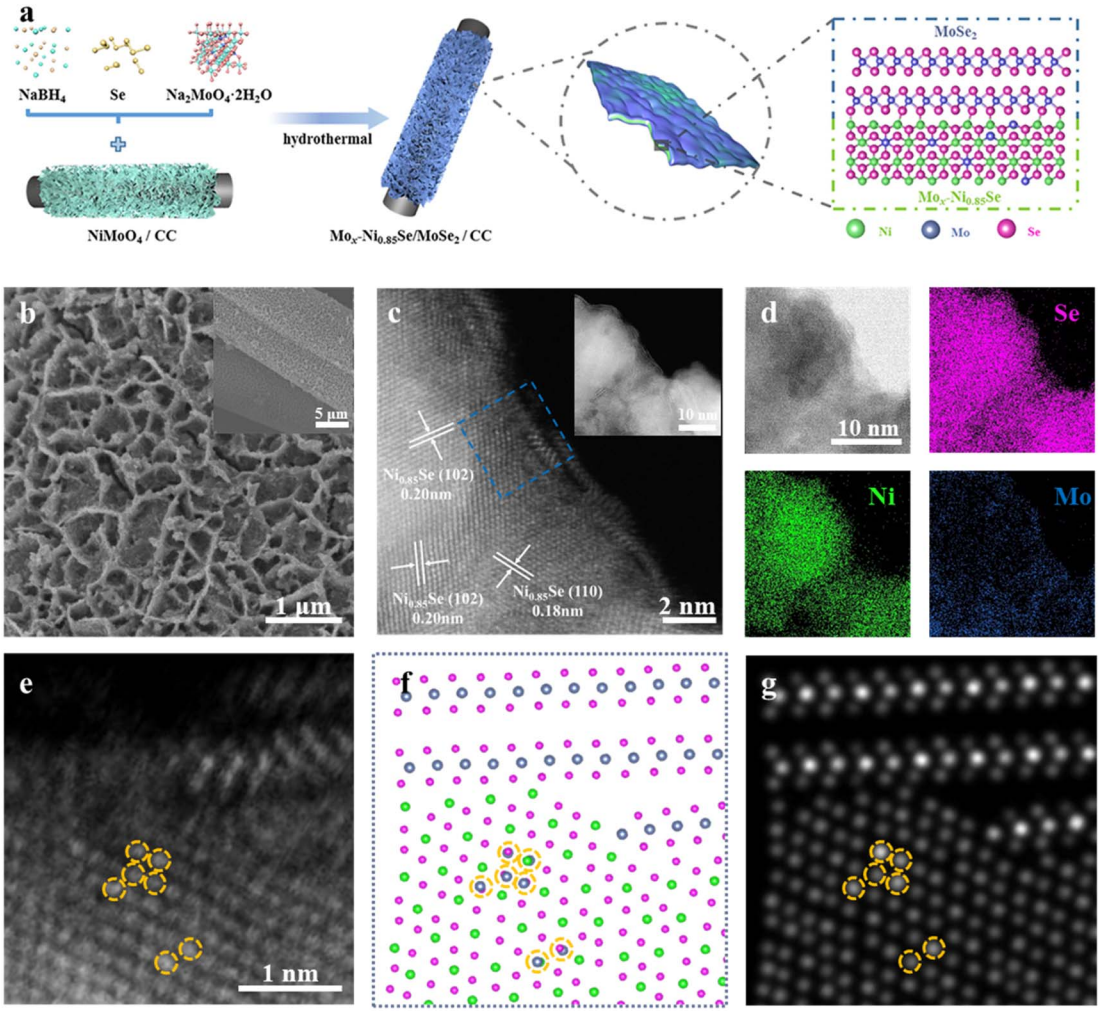

Fig. 1 The synthetic scheme and characterization of Mo_x-$Ni_{0.85}Se/MoSe_2$. (a) A schematic illustration for the synthesis of Mo_x-$N_{i0.85}Se/MoSe_2$. Low (inset) and high magnification (b) SEM, and (c) HAADF-STEM images of Mo_x-$N_{i0.85}Se/MoSe_2$. (d) Bright field STEM image and corresponding EDS elemental mapping of Mo_x-$N_{i0.85}Se/MoSe_2$. (e)-(g) From left to right are experimental HAADF-STEM image, structure model (Blue: Mo atom; Green: Ni atom; Red: Se atom), and simulated HAADF-STEM image of the selected area in (c), respectively.

fine structure (FT-EXAFS) spectra of the Ni K-edge for these samples are shown in Fig. 2d. The main peaks at 1.71 Å and 2.17 Å can be assigned to the Ni–Se coordination in $NiSe_2$, and the Ni–Ni coordination in Ni foil, respectively.[36] As for Mo_x-$Ni_{0.85}Se/MoSe_2$, the Ni–Se coordination exhibited was similar to that of $NiSe_2$, but the shift was in a positive direction, which was caused by the different bond lengths in Mo_x-$Ni_{0.85}Se/MoSe_2$.[36–38] The Mo K-edge XANES spectrum of Mo_x-$Ni_{0.85}Se/MoSe_2$ (Fig. 2b) showed a noticeable shift in the higher energy region compared to that of $MoSe_2$, which suggested there was a lower Mo chemical valency. The Mo EXAFS spectrum (Fig. 2e) of Mo_x-$Ni_{0.85}Se/MoSe_2$ showed the main peaks at 1.16 Å and 2.11 Å which were assigned to the Mo–Se coordination and Mo–Mo coordination, respectively.[39] The Mo–Mo peak of Mo_x-$Ni_{0.85}Se/MoSe_2$ was in agreement with that of $MoSe_2$ (2.11 Å), but the Mo–Se peak of Mo_x-$Ni_{0.85}Se/MoSe_2$ is positive shift 0.06 Å than that of $MoSe_2$ (1.22 Å), which could be attributed to the Mo cation doping in the $Ni_{0.85}Se$. The Se K-edge XANES for the Mo_x-$Ni_{0.85}Se/MoSe_2$ in Fig. 2c showed that it was more similar to that of $MoSe_2$, which suggested that they shared similar coordination environments to the Se element. The Se EXAFS spectra (Fig. 2f) indicated that the chemical environment of Se in Mo_x-$Ni_{0.85}Se/MoSe_2$ was similar to that in $MoSe_2$. To more clearly probe the coordination structures of the Mo_x-$Ni_{0.85}Se/MoSe_2$ epitaxially grown heterostructure, wavelet transforms (WT) with a high resolution in both the K and R spaces of the Ni K-edge and the Mo K-edge EXAFS oscillations were further performed and the results are shown in Fig. 2g, h and S10 (ESI).† Both the Ni and Mo in the Mo_x-$Ni_{0.85}Se/MoSe_2$ showed a certain degree of deviation, which indicated the change of the element coordination environment, resulting in the fast electron transfer in the heterostructure.[40,41] These results indicated that the heterogeneous structure of Mo_x-$Ni_{0.85}Se/MoSe_2$ may form an interfacial electric field, which facilitates the electron transfer.

The X-ray photoelectron spectroscopy (XPS) measurements (Fig. 2i–k, and S11, ESI†) were employed to further investigate the chemical and phase compositions. The Ni $2p_{3/2}$ XPS spectra of the Mo_x-$Ni_{0.85}Se/MoSe_2$ exhibited two peaks located at

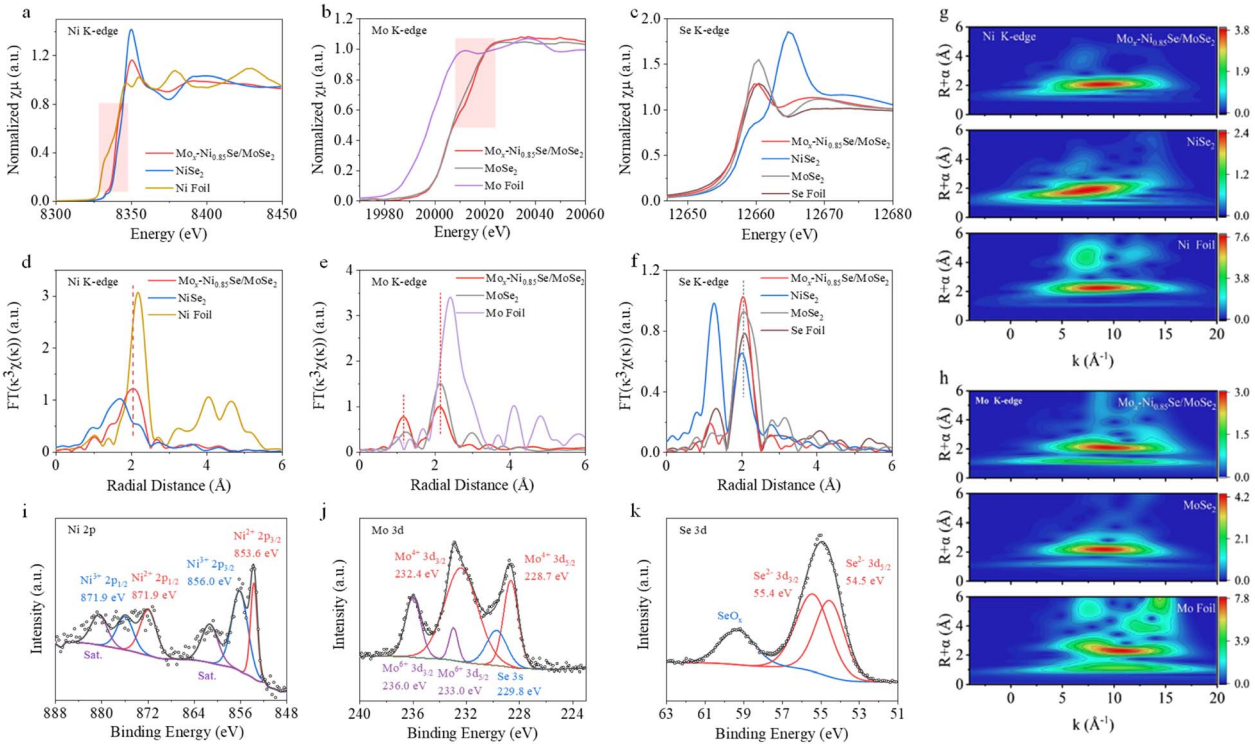

Fig. 2 Characterizations of Mo$_x$-Ni$_{0.85}$Se/MoSe$_2$. (a)–(c) The XANES spectra of Ni, Mo, and the Se K-edge, and (d)–(f) the corresponding FT-EXAFS spectra for Mo$_x$-Ni$_{0.85}$Se/MoSe$_2$, NiSe$_2$, MoSe$_2$, Ni foil, Mo foil, and Se foil. The wavelet transform of (g) the Ni K-edge and (h) the Mo K-edge EXAFS for Mo$_x$-Ni$_{0.85}$Se/MoSe$_2$, NiSe$_2$, Ni foil, MoSe$_2$, and Mo foil. The XPS spectra of (i) Ni 2p, (j) Mo 3d, and (k) Se 3d for Mo$_x$-Ni$_{0.85}$Se/MoSe$_2$.

853.6 eV (Ni^{2+} 2p$_{3/2}$) and 856.1 eV (Ni^{3+} 2p$_{3/2}$), which showed a slight decrease of ~0.2 eV when compared with that of pure Ni$_{0.85}$Se.[42] The Mo 3d$_{5/2}$ XPS spectra (Fig. 2j) can be divided into Mo^{4+} 3d$_{5/2}$ (228.7 eV) and Mo^{6+} 3d$_{5/2}$ (233.0 eV), and the Mo^{4+} 3d$_{5/2}$ showed an obvious increase of ~0.3 eV in Mo$_x$-Ni$_{0.85}$Se/MoSe$_2$ compared to that of pure MoSe$_2$.[43] This shift strongly suggested the presence of an interfacial electric field that serves to expedite the transfer of electrons from the MoSe$_2$ atomic layer to the Ni$_{0.85}$Se matrix. This observation significantly bolsters the evidence supporting the interaction between MoSe$_2$ and Ni$_{0.85}$Se within the Mo$_x$-Ni$_{0.85}$Se/MoSe$_2$ heterostructure. Moreover, the Se 3d spectrum showed two large peaks at 54.5 and 55.4 eV, which were attributed to Se^{2-} 3d$_{5/2}$ and Se^{2-} 3d$_{3/2}$. In addition, the binding energy of 59.5 eV could be attributed to SeO$_x$ resulting from the oxidation of the Se surface.[1,32]

The electrocatalytic HER performance of Mo$_x$-Ni$_{0.85}$Se/MoSe$_2$

The HER performance of Mo$_x$-Ni$_{0.85}$Se/MoSe$_2$ was evaluated in 1 M KOH with high-purity water and alkaline simulated seawater (1 M KOH and 0.5 M NaCl) using a three-electrode device (Fig. 3, and S12–S21, ESI†). It can be clearly seen that the Mo$_x$-Ni$_{0.85}$Se/MoSe$_2$ exhibited excellent HER performance in these two electrolytes, and only needed 110 mV to achieve 10 mA cm^{-2} in both 1 M KOH and alkaline simulated seawater. In contrast, NiSe$_2$ and MoSe$_2$ showed 147 mV@10 mA cm^{-2} and 211 mV@10 mA cm^{-2} in 1 M KOH, respectively. As for alkaline simulated seawater, NiSe$_2$ and MoSe$_2$ showed 160 mV@10 mA cm^{-2} and 232 mV@10 mA cm^{-2}, respectively. It was noted that, to a certain extent, the NiSe$_2$ could endure the Cl$^-$ poisoning, whereas the activity of MoSe$_2$ decreased significantly in the

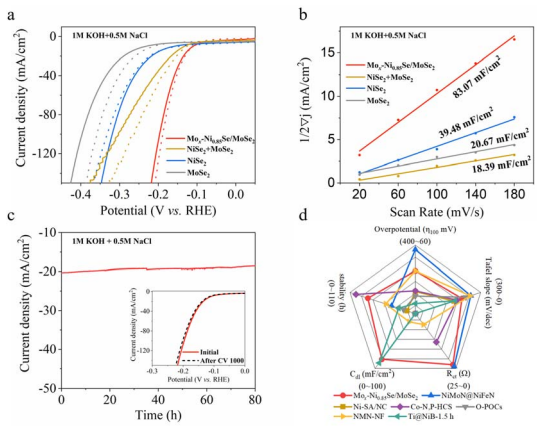

Fig. 3 The electrochemical properties of Mo$_x$-Ni$_{0.85}$Se/MoSe$_2$ catalyst. (a) Polarization curves. (b) The capacitive currents at −0.5 V *vs.* RHE as a function of the scan rate for the obtained catalysts. (c) Chronopotentiometry test results of the Mo$_x$-Ni$_{0.85}$Se/MoSe$_2$ catalyst at 20 mA cm^{-2} for 80 h (inset: LSV curves before and after 1000 cycles) in alkaline simulated seawater (1 M KOH + 0.5 M NaCl). (d) The electrochemical performance comparison between Mo$_x$-Ni$_{0.85}$Se/MoSe$_2$ and previously reported values obtained in alkaline simulated seawater, found in the literature .

presence of Cl^-. The physical mixed $NiSe_2$ and $MoSe_2$ (named as $NiSe_2$ + $MoSe_2$) showed 126 mV@10 mA cm^{-2} (1 M KOH) and 132 mV@10 mA cm^{-2} (alkaline simulated seawater), suggesting that the physical mixture cannot efficiently endure the Cl^- poisoning. These results demonstrated that the Mo_x-$Ni_{0.85}Se$/$MoSe_2$ heterostructure showed an excellent performance in alkaline simulated seawater which should be attributed to the heterostructure structure. In addition, the Mo cation in Mo_x-$Ni_{0.85}Se/MoSe_2$ will also modify its local electronic structure, and thus enhanced the electron transfer between Mo_x-$Ni_{0.85}Se$ and $MoSe_2$ in the heterostructure.

The Tafel slope values of Mo_x-$Ni_{0.85}Se/MoSe_2$ in 1 M KOH and alkaline simulated seawater (Fig. S14, ESI†) are the lowest among these catalysts and were 70.12 and 86.19 mV dec^{-1}, respectively. This indicated the favorable kinetics of the Mo_x-$Ni_{0.85}Se/MoSe_2$ during the electrocatalytic hydrogen production process, even in the presence of Cl^-. Moreover, the value of the Tafel slope of Mo_x-$Ni_{0.85}Se/MoSe_2$ is between the Volmer mechanism (120 mV dec^{-1}) and the Heyrovský mechanism (40 mV dec^{-1}), which indicated that it most likely obeys the Volmer–Heyrovský mechanism.[1,44,45] This was in agreement with previous reports where nickel chalcogenides were found to be efficient to produce had in the water dissociation process (Volmer step), resulting in H_{ad} migrating to the neighboring active site of $MoSe_2$ to undergo the Heyrovský mechanism to produce H_2O molecules.[44,46,47] The electrochemical impedance spectroscopy (EIS) at an overpotential of 250 mV revealed that the Mo_x-$Ni_{0.85}Se/MoSe_2$ has the lowest charge transfer resistance of 1.749 Ω in 1 M KOH (Fig. S15, ESI†) and 1.508 Ω in alkaline simulated seawater (Fig. S16, ESI†) when compared with the other three electrocatalysts. This implied its quick charge transfer capability, which could be attributed to the built-in interfacial electric field of $Ni_{0.85}Se/MoSe_2$ heterostructure and the Mo cation doping, and this was in agreement with the XAS and XPS results.

To obtain insights into the electrochemical surface area (ECSA) of the materials, the electrochemical double-layer capacitance (C_{dl}) values were estimated and are shown in Fig. 3b, S17 and S18 (ESI).† The Mo_x-$Ni_{0.85}Se/MoSe_2$ had the highest C_{dl} value of 92.97 mF cm^{-2} in 1 M KOH, and this indicated that it had a larger electrocatalytic active surface area. However, this decreased to 83.07 mF cm^{-2} in alkaline simulated seawater. This result suggested that the Cl^- will slightly influence the electrochemistry of Mo_x-$Ni_{0.85}Se/MoSe_2$. The previously mentioned results demonstrated that the Mo_x-$Ni_{0.85}Se$/$MoSe_2$ was an excellent electrocatalyst even in alkaline simulated seawater. However, in the practical application of electrocatalysts, stability is another important parameter, especially in the alkaline simulated seawater environment, due to the fact that the Cl^- can cause electrocatalyst poisoning and corrosion. The cyclic voltammetry (CV) was performed for 1000 cycles and the *i*–*t* mode was performed at 20 mA cm^{-2} for a continuous 80 h Mo_x-$Ni_{0.85}Se/MoSe_2$ in alkaline simulated seawater (Fig. 3c). It can be clearly seen that after 80 h, the current density of Mo_x-$Ni_{0.85}Se/MoSe_2$ only showed a slight decrease, as shown in the inset of Fig. 3c, after 1000 CV cycles, and the linear sweep voltammetry (LSV) curve of Mo_x-$Ni_{0.85}Se/MoSe_2$ was almost unchanged. Moreover, after 1000 CV cycles, the Mo_x-$Ni_{0.85}Se$/$MoSe_2$ can maintain its structure (Fig. S21, ESI†). Both these results illustrated that the Mo*x*-$Ni_{0.85}Se/MoSe_2$ has the ability for anti-Cl ion corrosion, and a great performance even in alkaline simulated seawater. The radar chart (Fig. 3d) and the comparison with results reported in the literature (Table S1, ESI†) showed that the integrated HER performance of Mo_x-$Ni_{0.85}Se/MoSe_2$ exhibited the best HER performance in alkaline simulated seawater.

Thus, the role of Mo cation doping has two distinct functions: firstly, it enhances the charge transfer capability of the built-in interfacial electric field within the $Ni_{0.85}Se/MoSe_2$ heterostructure; secondly, the Mo cation doping can also modulate the local electronic state of Ni, effectively enabling the resistance against chloride ions in alkaline seawater solutions and safeguarding the electrode materials from chloride ion corrosion.

Mechanism of cation tuning

The first-principles calculations were adopted to evaluate the effects of Mo absorption, and the $MoSe_2$/NiSe heterojunction. The absorption energies of H_2O on NiSe and Mo-NiSe (Fig. S22, ESI†) were −0.88 and −0.70 eV, respectively. The water dissociation barrier for NiSe was 3.02 eV (Fig. S23a, ESI†), however, the Mo cation doping of Mo-NiSe increased it to 3.08 eV. This indicated that the Mo substitution did not directly enhance the water dissociation. As for the $MoSe_2$/NiSe heterojunction, its water dissociation barrier was 2.72 eV, which was much lower than that of NiSe (3.02 eV) as shown in Fig. S23b (ESI),† indicating the great performance of $MoSe_2$/NiSe for hydrogen evolution. The lower water dissociation barrier of the $MoSe_2$/NiSe heterojunction could be attributed to its built-in interfacial electric field, which facilitated the charge-transfer.

The resistance to Cl^- corrosion for these samples was evaluated and the results are shown in Fig. 4. The absorption energy of H_2O around the Cl adatom on the surface of the NiSe + Cl increased from −0.88 eV to −0.19 eV, indicating that the Cl absorption hinders the H_2O absorption. Fig. 4a–c show that the Cl atom can only be absorbed on the top of the Se atom on the surface of NiSe (referred to as NiSe + Cl), whereas the Cl atoms can be absorbed on both the Se and Mo on the surface of Mo-NiSe (referred to as Mo-NiSe + Cl_1 and Mo-NiSe + Cl_2, respectively). The absorption energies (G_{abs}) were −0.54, −0.06, and −0.26 eV for NiSe + Cl, Mo-NiSe + Cl_1, and Mo-NiSe + Cl_2, respectively, as shown in Fig. 4g. The increased G_{abs} when compared to NiSe indicated that there was a resistance to Cl-ion corrosion after the Mo doping of NiSe. To explain this phenomenon, the charge density difference (ρ_{diff}) and the projected density of states (PDOS) were calculated (Fig. 4 and S24, ESI†).

As shown in Fig. 4d–f, a polar covalent bond was formed between the Cl adatom and the Se atom in both NiSe + Cl and Mo-NiSe + Cl1, whereas an ionic bond was formed between the Cl adatom and the Mo atom in Mo-NiSe + Cl2. From Fig. S24 (ESI),† it can be seen that the bonding interaction arose from

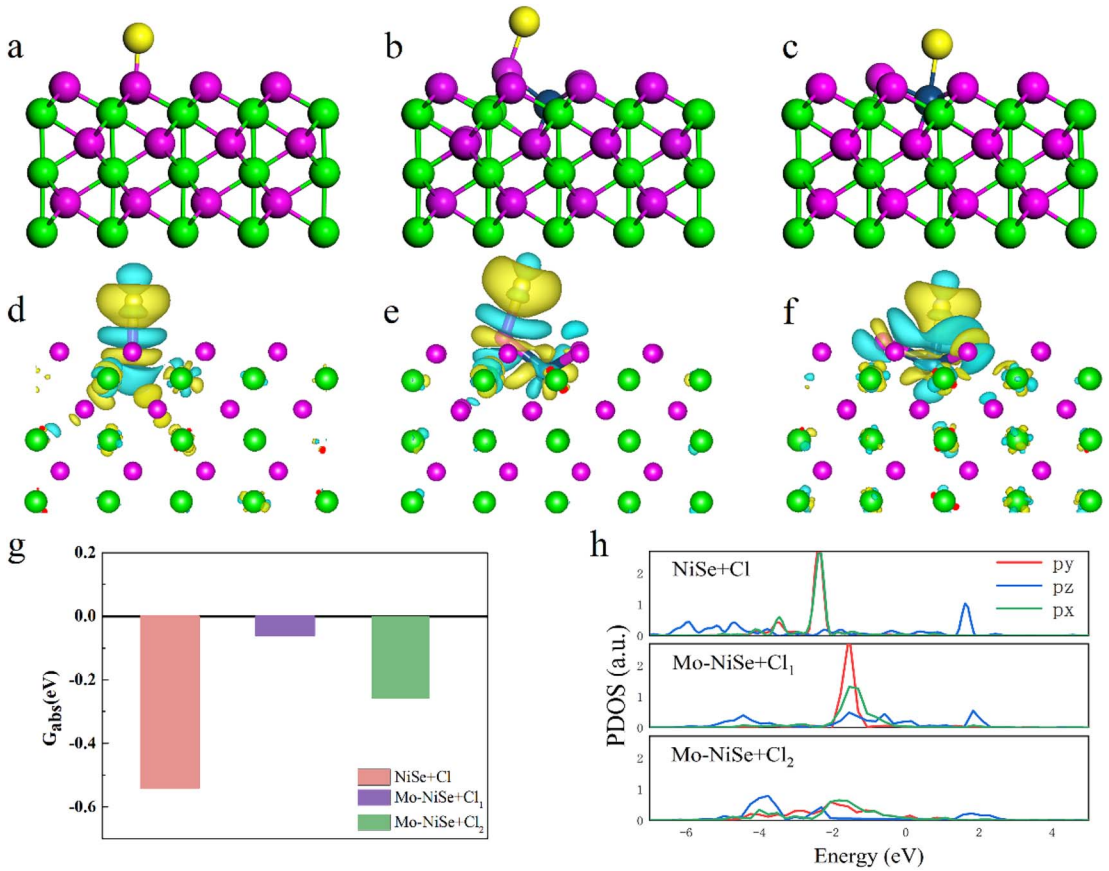

Fig. 4 Mechanistic studies using DFT. (a)–(c) Schematic diagrams of the atomic structure of NiSe + Cl, Mo-NiSe + Cl_1, and Mo-NiSe + Cl_2. (d)-(f) Distribution of ρ_{diff} in NiSe + Cl, Mo-NiSe + Cl_1, and Mo-NiSe + Cl_2. The isosurface level is set to 10^{-3}. (g) and (h) The absorption energies and the PDOS of the Cl adatom in NiSe + Cl, Mo-NiSe + Cl_1, and Mo-NiSe + Cl_2, respectively.

the resonance between the Cl_pz and Se_pz states in both NiSe + Cl and Mo-NiSe + Cl1, whereas the bonding interaction corresponded to the coupling between the Cl_pz and the Mo_dz^2 in Mo-NiSe + Cl_2. Compared to NiSe + Cl, a considerable shifting of the bonding state towards the Fermi level was found in Mo-NiSe + Cl_1 and Mo-NiSe + Cl_2 (Fig. 4h), and this indicated a weakening of the bonding interaction strength between the Cl adatom and the surface atom. The variation in the strength of the bonding interaction is related to the difference in the coordination environment between Mo and Ni, which modifies the crystal field splitting and orbital hybridization. As shown in Fig. 4a, the Ni atom bonds with six neighboring Se atoms, forming an octahedral geometry. In this octahedral geometry, the d orbitals form sp^3d^2 hybridization, and the Ni exhibits a valency of +2. However, the Mo atom bonds with five neighboring Se atoms (Fig. 4b), forming a square pyramidal geometry. In this structure, the d orbitals form sp^3d hybridization, and the Mo exhibits a valency of +3. The variation of the valency influences the charge transfer and weakens the bonding interaction between the Cl and Se in Mo-NiSe + Cl_1. In the Mo-NiSe + Cl_2, the Cl–Mo direction did not align with the Mo_4d hybrid orbitals, indicating that the Cl–Mo direction was not suitable for electron pairing to form a chemical bond. Consequently, only a weak ionic bond was formed between the Cl and Mo atoms in Mo-NiSe + Cl_2.

Conclusions

In summary, a convenient strategy to synthesize Mo_x-$Ni_{0.85}Se$/$MoSe_2$ nanosheet network heterostructures supported on carbon cloth has been successfully developed by the selenization of the $NiMoO_4$ nanosheets precursor. The STEM and XAS results demonstrate that the atomic $MoSe_2$ nanosheets were grown epitaxially at the edge of the Mo_x-$Ni_{0.85}Se$, and the Mo cation doping tuned the local electronic environment of the Mo_x-$Ni_{0.85}Se/MoSe_2$ heterostructures. This exhibits an excellent performance for HER in alkaline simulated seawater with a low overpotential of 110 mV at the current density of 10 mA cm^{-2}, and shows almost no sign of waning even after 80 h at 20 mA cm^{-2}. The excellent HER performance in alkaline simulated seawater could be attributed to the built-in interfacial electric field of the Mo_x-$Ni_{0.85}Se/MoSe_2$ heterostructure and Mo cation doping, that improves the electron transfer between adsorbed species and Mo_x-$Ni_{0.85}Se/MoSe_2$. Moreover, the Mo cation doping also weakens the bonding interaction between Cl–Se and Cl–Mo, thereby protecting it against the poisoning and erosion of chloride ions.

Data availability

The authors confirm that the data supporting the findings of this study are available within the article ESI.†

Author contributions

ZH, CZ, and SG contributed equally to this manuscript. BZ and YL supervised this study. BZ, YL, and ZH conceived the idea. ZH and YJ planned and carried out the experiments, and collected and analyzed the experimental data. SG and NC performed SEM and TEM characterizations. SL performed the Raman characterizations. CZ conducted the theoretical calculations. BZ and ZH wrote the paper. All the authors have discussed the results and wrote the paper together.

Conflicts of interest

The authors declare that they have no competing interests.

Acknowledgements

This work was supported by the National Natural Science Foundation of China (Grant No. 12004321, 22279011, 52201003), the Fundamental Research Funds for the Central Universities (Grant No. 2023CDJXY-046), the Scientific Research Project of Hunan Provincial Education Department (Grant No. 23B0157), and the Program for Changjiang Scholars and Innovative Research Team in University (Grant No. IRT17R91).

Notes and references

1 Y. Ji, W. J. Luo, Y. D. Liu, Z. M. He, N. Y. Cheng, Z. Zhang, X. Qi, J. X. Zhong and L. Ren, Bifunctional o-$CoSe_2$/c-$CoSe_2$/$MoSe_2$ heterostructures for enhanced electrocatalytic and photoelectrochemical hydrogen evolution reaction, *Mater. Today Chem.*, 2022, **23**, 100724.

2 M. Zhu, Q. Yan, Y. Q. Xue, Y. D. Yan, K. Zhu, K. Ye, J. Yan, D. X. Cao, H. J. Xie and G. L. Wang, Free-standing P-doped $NiSe_2$/$MoSe_2$ catalyst for efficient hydrogen evolution in acidic and alkaline media, *ACS Sustain. Chem. Eng.*, 2021, **10**, 279–287.

3 L. Wu, F. H. Zhang, S. W. Song, M. H. Ning, Q. Zhu, J. Q. Zhou, G. H. Gao, Z. Y. Chen, Q. C. Zhou and X. X. Xing, Efficient alkaline water/seawater hydrogen evolution by a nanorod-nanoparticle-structured Ni-MoN catalyst with fast water-dissociation kinetics, *Adv. Mater.*, 2022, **34**, 2201774.

4 J. X. Guo, Y. Zheng, Z. P. Hu, C. Y. Zheng, J. Mao, K. Du, M. Jaroniec, S. Z. Qiao and T. Ling, Direct seawater electrolysis by adjusting the local reaction environment of a catalyst, *Nat. Energy*, 2023, **8**, 264–272.

5 M. Khan, T. Al-Attas, S. Roy, M. M. Rahman, N. Ghaffour, V. Thangadurai, S. Larter, J. Hu, P. M. Ajayan and M. G. Kibria, Seawater electrolysis for hydrogen production: a solution looking for a problem?, *Energy Environ. Sci.*, 2021, **14**, 4831–4839.

6 S. r. Dresp, F. Dionigi, M. Klingenhof and P. Strasser, Direct electrolytic splitting of seawater: opportunities and challenges, *ACS Energy Lett.*, 2019, **4**, 933–942.

7 B. H. Suryanto, Y. Wang, R. K. Hocking, W. Adamson and C. Zhao, Overall electrochemical splitting of water at the heterogeneous interface of nickel and iron oxide, *Nat. Commun.*, 2019, **10**, 5599.

8 J. N. Hausmann, R. Schlögl, P. W. Menezes and M. Driess, Is direct seawater splitting economically meaningful?, *Energy Environ. Sci.*, 2021, **14**, 3679–3685.

9 F. Sun, J. S. Qin, Z. Y. Wang, M. Z. Yu, X. H. Wu, X. Sun and J. S. Qiu, Energy-saving hydrogen production by chlorine-free hybrid seawater splitting coupling hydrazine degradation, *Nat. Commun.*, 2021, **12**, 4182.

10 Y. Y. Guo, Y. H. Cao, J. D. Lu, X. R. Zheng and Y. D. Deng, The concept, structure, and progress of seawater metal-air batteries, *Microstructures*, 2023, **3**, 2023038.

11 X. Y. Lu, J. Pan, E. Lovell, T. H. Tan, Y. H. Ng and R. Amal, A sea-change: Manganese doped nickel/nickel oxide electrocatalysts for hydrogen generation from seawater, *Energy Environ. Sci.*, 2018, **11**, 1898–1910.

12 Y. Kuang, M. J. Kenney, Y. Meng, W.-H. Hung, Y. Liu, J. E. Huang, R. Prasanna, P. Li, Y. Li and L. Wang, Solar-driven, highly sustained splitting of seawater into hydrogen and oxygen fuels, *Proc. Natl. Acad. Sci. U. S. A.*, 2019, **116**, 6624–6629.

13 F. Dionigi, T. Reier, Z. Pawolek, M. Gliech and P. Strasser, Design criteria, operating conditions, and nickel–iron hydroxide catalyst materials for selective seawater electrolysis, *ChemSusChem*, 2016, **9**, 962–972.

14 W. J. Zang, T. Sun, T. Yang, S. B. Xi, M. Waqar, Z. K. Kou, Z. Y. Lyu, Y. P. Feng, J. Wang and S. J. Pennycook, Efficient hydrogen evolution of oxidized Ni-N_3 defective sites for alkaline freshwater and seawater electrolysis, *Adv. Mater.*, 2021, **33**, 2003846.

15 D. Liu, H. Q. Ai, M. P. Chen, P. F. Zhou, B. W. Li, D. Liu, X. Y. Du, K. Lo, K. Ng and S. P. Wang, Multi-phase heterostructure of CoNiP/CoxP for enhanced hydrogen evolution under alkaline and seawater conditions by promoting H_2O dissociation, *Small*, 2021, **17**, 2007557.

16 B. W. Zhang, L. Ren, Z. F. Xu, N. Y. Cheng, W. H. Lai, L. Zhang, W. Hao, S. Q. Chu, Y. X. Wang and Y. Du, Atomic Structural Evolution of Single-Layer Pt Clusters as Efficient Electrocatalysts, *Small*, 2021, **17**, 2100732.

17 B. W. Zhang, H. L. Yang, Y. X. Wang, S. X. Dou and H. K. Liu, A comprehensive review on controlling surface composition of Pt-based bimetallic electrocatalysts, *Adv. Energy Mater.*, 2018, **8**, 1703597.

18 B. W. Zhang, Y. X. Wang, S. L. Chou, H. K. Liu and S. X. Dou, Fabrication of superior single-atom catalysts toward diverse electrochemical reactions, *Small Methods*, 2019, **3**, 1800497.

19 J. H. Zheng, J. L. Zhang, G. Li, J. M. Zhang, B. W. Zhang, Y. X. Jiang and S. G. Sun, Tuning atomic Pt site surface on PtAu alloy toward electro-oxidation of formic acid, *Mater. Today Energy*, 2022, **27**, 101028.

20 J. H. Zheng, G. Li, J. M. Zhang, N. Y. Cheng, L. F. Ji, J. Yang, J. L. Zhang, B. W. Zhang, Y. X. Jiang and S. G. Sun, General strategy for evaluating the d-band center shift and ethanol oxidation reaction pathway towards Pt-based electrocatalysts, *Sci. China: Chem.*, 2023, **66**, 279–288.

21 W. Tong, M. Forster, F. Dionigi, S. Dresp, R. Sadeghi Erami, P. Strasser, A. J. Cowan and P. Farràs, Electrolysis of low-grade and saline surface water, *Nat. Energy*, 2020, **5**, 367–377.

22 W. Chen, J. Pei, C. T. He, J. Wan, H. Ren, Y. Zhu, Y. Wang, J. Dong, S. Tian and W. C. Cheong, Rational design of single molybdenum atoms anchored on N-doped carbon for effective hydrogen evolution reaction, *Angew. Chem.*, 2017, **129**, 16302–16306.

23 J. Mahmood, F. Li, S. M. Jung, M. S. Okyay, I. Ahmad, S. J. Kim, N. Park, H. Y. Jeong and J. B. Baek, An efficient and pH-universal ruthenium-based catalyst for the hydrogen evolution reaction, *Nat. Nanotechnol.*, 2017, **12**, 441–446.

24 Y. Jiao, Y. Zheng, K. Davey and S. Z. Qiao, Activity origin and catalyst design principles for electrocatalytic hydrogen evolution on heteroatom-doped graphene, *Nat. Energy*, 2016, **1**, 1–9.

25 Y. Q. Zhao, B. Jin, Y. Zheng, H. Y. Jin, Y. Jiao and S. Z. Qiao, Charge state manipulation of cobalt selenide catalyst for overall seawater electrolysis, *Adv. Energy Mater.*, 2018, **8**, 1801926.

26 B. S. Zhang, W. W. Xu, S. Liu, X. Chen, T. F. Ma, G. H. Wang, Z. Y. Lu and J. Sun, Enhanced interface interaction in Cu_2S@Ni core-shell nanorod arrays as hydrogen evolution reaction electrode for alkaline seawater electrolysis, *J. Power Sources*, 2021, **506**, 230235.

27 C. Z. Wang, M. Z. Zhu, Z. Y. Cao, P. Zhu, Y. Q. Cao, X. Y. Xu, C. X. Xu and Z. Y. Yin, Heterogeneous bimetallic sulfides based seawater electrolysis towards stable industrial-level large current density, *Appl. Catal., B*, 2021, **291**, 120071.

28 Y. Li, X. Bao, D. Chen, Z. Wang, N. Dewangan, M. Li, Z. Xu, J. Wang, S. Kawi and Q. Zhong, A Minireview on Nickel-Based Heterogeneous Electrocatalysts for Water Splitting, *ChemCatChem*, 2019, **11**, 5913–5928.

29 R. Andaveh, A. Sabour Rouhaghdam, J. Ai, M. Maleki, K. Wang, A. Seif, G. Barati Darband and J. Li, Boosting the electrocatalytic activity of NiSe by introducing MnCo as an efficient heterostructured electrocatalyst for large-current-density alkaline seawater splitting, *Appl. Catal., B*, 2023, **325**, 122355.

30 L. Zhang, T. Wang, L. Sun, Y. J. Sun, T. W. Hu, K. W. Xu and F. Ma, Hydrothermal synthesis of 3D hierarchical $MoSe_2$/$NiSe_2$ composite nanowires on carbon fiber paper and their enhanced electrocatalytic activity for the hydrogen evolution reaction, *J. Mater. Chem. A*, 2017, **5**, 19752–19759.

31 X. Q. Wang, B. J. Zheng, B. Wang, H. Q. Wang, B. C. Sun, J. R. He, W. L. Zhang and Y. F. Chen, Hierarchical $MoSe_2$-$CoSe_2$ nanotubes anchored on graphene nanosheets: A highly efficient and stable electrocatalyst for hydrogen evolution in alkaline medium, *Electrochim. Acta*, 2019, **299**, 197–205.

32 J. Y. Xue, F. L. Li, B. B. Chen, H. B. Geng, W. Zhang, W. Y. Xu, H. W. Gu, P. Braunstein and J. P. Lang, Engineering multiphasic $MoSe_2$/NiSe heterostructure interfaces for superior hydrogen production electrocatalysis, *Appl. Catal., B*, 2022, **312**, 121434.

33 C. Koch, *Determination of core structure periodicity and point defect density along dislocations*, Arizona State University, 2002.

34 Z. D. Huang, B. Xu, Z. G. Li, J. W. Ren, H. Mei, Z. N. Liu, D. G. Xie, H. B. Zhang, F. Dai and R. Wang, Accurately Regulating the Electronic Structure of Ni_xSe_y@ NC Core–Shell Nanohybrids through Controllable Selenization of a Ni-MOF for pH-Universal Hydrogen Evolution Reaction, *Small*, 2020, **16**, 2004231.

35 S. Setayeshgar, M. Karimipour, M. Molaei, M. R. Moghadam and S. Khazraei, Synthesis of scalable 1T/2H–$MoSe_2$ nanosheets with a new source of Se in basic media and study of their HER activity, *Int. J. Hydrogen Energy*, 2020, **45**, 6090–6101.

36 S. L. Han, Y. N. Hao, Z. Y. Guo, D. S. Yu, H. J. Huang, F. Hu, L. L. Li, H. Y. Chen and S. J. Peng, Self-supported N-doped $NiSe_2$ hierarchical porous nanoflake arrays for efficient oxygen electrocatalysis in flexible zinc-air batteries, *Chem. Eng. J.*, 2020, **401**, 126088.

37 Y. C. Chu, C. J. Chang, Y. P. Zhu, S. C. Lin, C. W. Tung, T. L. Chen and H. M. Chen, Anionic effects on metal pair of Se-doped nickel diphosphide for hydrogen evolution reaction, *ACS Sustain. Chem. Eng.*, 2019, 7, 14247–14255.

38 S. J. Shen, Z. P. Lin, K. Song, Z. P. Wang, L. G. Huang, L. H. Yan, F. Q. Meng, Q. H. Zhang, L. Gu and W. W. Zhong, Reversed active sites boost the intrinsic activity of graphene-like cobalt selenide for hydrogen evolution, *Angew. Chem.*, 2021, **133**, 12468–12473.

39 I. S. Kwon, I. H. Kwak, J. Y. Kim, T. T. Debela, Y. C. Park, J. Park and H. S. Kang, Concurrent Vacancy and Adatom Defects of $Mo_{1-x}Nb_xSe_2$ Alloy Nanosheets Enhance Electrochemical Performance of Hydrogen Evolution Reaction, *ACS Nano*, 2021, **15**, 5467–5477.

40 Y. Cheng, H. R. Guo, X. P. Li, X. Wu, X. H. Xu, L. R. Zheng and R. Song, Rational design of ultrahigh loading metal single-atoms (Co, Ni, Mo) anchored on in-situ pre-crosslinked guar gum derived N-doped carbon aerogel for efficient overall water splitting, *Chem. Eng. J.*, 2021, **410**, 128359.

41 W. Wan, Y. Zhao, S. Wei, C. A. Triana, J. Li, A. Arcifa, C. S. Allen, R. Cao and G. R. Patzke, Mechanistic insight into the active centers of single/dual-atom Ni/Fe-based oxygen electrocatalysts, *Nat. Commun.*, 2021, **12**, 5589.

42 D. Chen, J. W. Shen, X. Li, S. A. Cao, T. Li, W. Luo and F. Xu, $Ni_{0.85}Se$ hexagonal nanosheets as an advanced conversion cathode for Mg secondary batteries, *J. Energy Chem.*, 2020, **48**, 226–232.

43 H. Tang, H. Huang, X. Wang, K. Wu, G. Tang and C. Li, Hydrothermal synthesis of 3D hierarchical flower-like $MoSe_2$ microspheres and their adsorption performances for methyl orange, *Appl. Surf. Sci.*, 2016, **379**, 296–303.

44 H. R. Inta, S. Ghosh, A. Mondal, G. Tudu, H. V. Koppisetti and V. Mahalingam, $Ni_{0.85}Se$/$MoSe_2$ interfacial structure: an efficient electrocatalyst for alkaline hydrogen evolution reaction, *ACS Appl. Energy Mater.*, 2021, **4**, 2828–2837.

45 R. Qin, J. G. Hou, C. X. Xu, H. X. Yang, Q. X. Zhou, Z. Z. Chen and H. Liu, Self-supporting $Co_{0.85}Se$ nanosheets anchored on Co plate as highly efficient electrocatalyst for hydrogen evolution reaction in both acidic and alkaline media, *Nano Res.*, 2020, **13**, 2950–2957.

46 X. Zhang, Y. Y. Zhang, Y. Zhang, W. J. Jiang, Q. H. Zhang, Y. G. Yang, L. Gu, J. S. Hu and L. J. Wan, Phase-controlled synthesis of 1T-$MoSe_2$/NiSe heterostructure nanowire arrays via electronic injection for synergistically enhanced hydrogen evolution, *Small Methods*, 2019, **3**, 1800317.

47 H. Ding, Q. Y. Jiao, H. F. Lv, K. Xu, Q. Y. Xing, M. Chen, W. S. Chu, X. J. Wu and Y. Q. Guo, Promoting the water reduction reaction of transition metal dichalcogenides in a basic electrolyte by interface engineering, *J. Mater. Chem. A*, 2018, **6**, 17488–17494.